

## 3D imaging of a reservoir analogue in point bar deposits in the Ferron Sandstone, Utah, using ground-penetrating radar

Xiaoxian Zeng, George A. McMechan,\* Janok P. Bhattacharya, Carlos L.V. Aiken, Xueming Xu, William S. Hammon III and Rucsandra M. Corbeanu

*Center for Lithospheric Studies, University of Texas at Dallas, PO Box 830688, Richardson, TX 75083-0688, USA*

Received August 2001, revision accepted August 2003

### ABSTRACT

Most existing reservoir models are based on 2D outcrop studies; 3D aspects are inferred from correlation between wells, and so are inadequately constrained for reservoir simulations. To overcome these deficiencies, we have initiated a multidimensional characterization of reservoir analogues in the Cretaceous Ferron Sandstone in Utah. Detailed sedimentary facies maps of cliff faces define the geometry and distribution of reservoir flow units, barriers and baffles at the outcrop. High-resolution 2D and 3D ground-penetrating radar (GPR) images extend these reservoir characteristics into 3D to allow the development of realistic 3D reservoir models. Models use geometric information from mapping and the GPR data, combined with petrophysical data from surface and cliff-face outcrops, and laboratory analyses of outcrop and core samples.

The site of the field work is Corbula Gulch, on the western flank of the San Rafael Swell, in east-central Utah. The outcrop consists of an 8–17 m thick sandstone body which contains various sedimentary structures, such as cross-bedding, inclined stratification and erosional surfaces, which range in scale from less than a metre to hundreds of metres. 3D depth migration of the common-offset GPR data produces data volumes within which the inclined surfaces and erosional surfaces are visible. Correlation between fluid permeability, clay content, instantaneous frequency and instantaneous amplitude of the GPR data provides estimates of the 3D distribution of fluid permeability and clay content.

### INTRODUCTION

This multidisciplinary project applies ground-penetrating radar (GPR) for 3D characterization of the internal geometry of a clastic reservoir analogue. The site is in the Ferron Sandstone at Corbula Gulch, which is about 16 km south of Emery in east-central Utah (Fig. 1). The site consists of an accessible mesa top with cliff-face exposures on two sides as well as outcrop on the mesa top (Fig. 2a). The outcrop clearly shows a lateral accretion set, channels and cross-bedding, on scales of less than a metre to hundreds of metres (Fig. 3). The acquired data (refer to Fig. 2b) include global-positioning system (GPS) data for the 3D topography and locations of all the measure-

ments, core plugs from the cliff faces, stratigraphic sections, gamma-ray profiles, lasergun mapping of bounding surfaces, detailed sedimentological mapping, palaeocurrent directions, and drilling of continuous cores to an average of 16 m depth in four holes, as well as acquisition of two 3D GPR volumes and two scales of 2D GPR grids (450 × 650 m and 100 × 150 m). A summary of the results of integration of these geophysical and geological data and the construction of the reservoir analogue is the core of this paper.

One key difference between this paper and others that have similar goals (e.g. Szerbiak, McMechan and Corbeanu 2001) is that the procedures here are deterministic rather than statistical wherever possible. This paper concentrates on the surface 2D and 3D GPR data. Other aspects are detailed in other papers: the sedimentology is presented by Corbeanu *et al.* (2004);

---

\*E-mail: mcmec@utdallas.edu

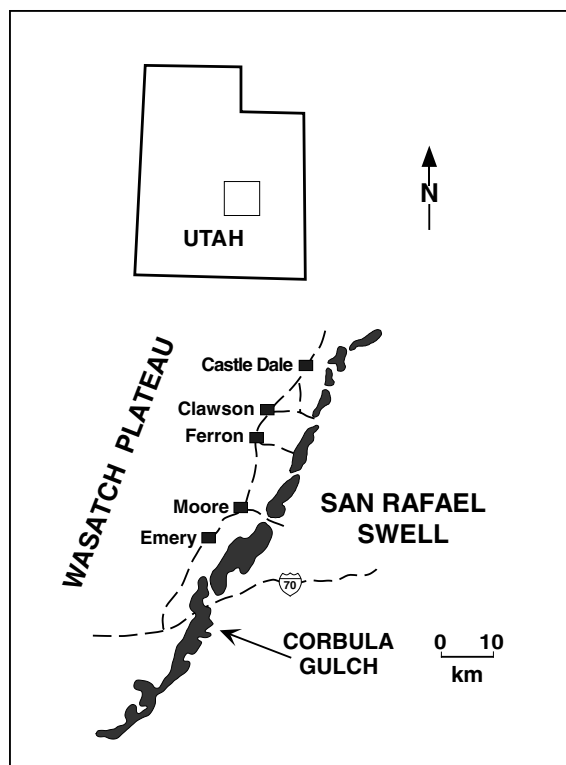


**Figure 1** Location of Corbula Gulch. Utah is in the west-central United States. The shaded areas are the surface outcrops of the Ferron Sandstone.

analysis of the borehole GPR data is presented by Hammon *et al.* (2002); estimation of permeability and clay volumes is presented by Corbeanu *et al.* (2002); the laser mapping and GPS results are presented by Xu *et al.* (2001); the fluid-flow modelling is presented by Novakovic *et al.* (2002).

### Site surveys

To obtain topographic data with the accuracy required for this project, we needed to produce our own. The site contains steep, and in some places overhanging, cliff faces, so it is necessary to obtain a truly 3D representation of the topography as the basis of the outcrop mapping. This was achieved by a combination of GPS and Laser Ranging data. The laser system served as a total station, which gives the local offset relative to the shooting station, while GPS locates the shooting station so that the local laser points can be globally referenced. An advantage of the laser ranging system is that geological features can be rapidly traced (in 3D) without having to visit the target. A real-time kinematic (RTK) GPS provides accuracy close to the maximum achievable by any GPS method, and does so in real-time (Langley 1998) using carrier-phase dif-

ferential positioning. Details for the present project are given by Xu *et al.* (2001). The resulting topographic surface is shown in Fig. 2(a); the locations of the GPR and other data points, lines and volumes are shown in Fig. 2(b).

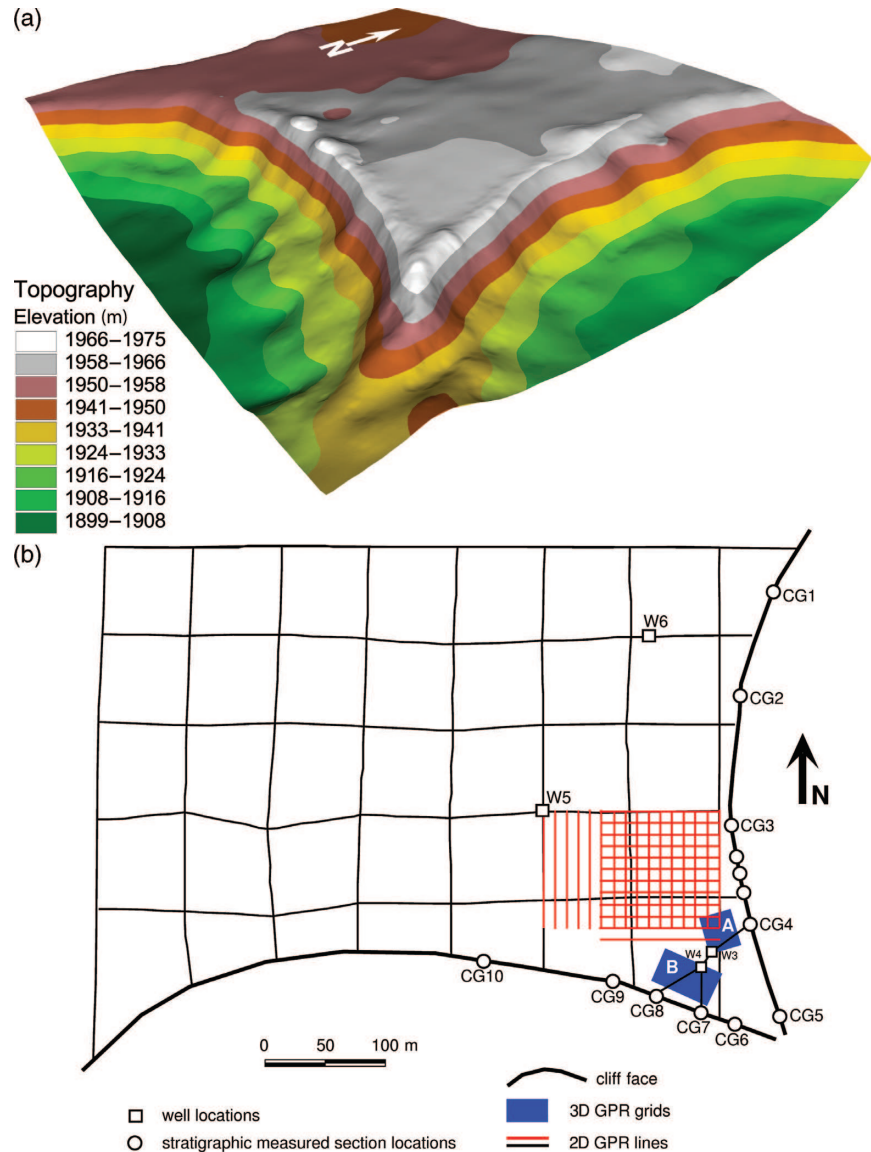
### Geological setting

The mid-Cretaceous Ferron Sandstone consists of fluvio-deltaic sediments within deltas that prograded towards the northeast over a distance of more than 100 km. At present, the Ferron Delta complex is exposed as a series of sandstone cliffs along the western flank of the San Rafael Swell (Fig. 1). Originally the delta complex covered more than 8000 km<sup>2</sup>. Since the scale and depositional setting of the Ferron is considered an analogue for many oilfields, its exposures have been subject to intensive analysis by petroleum reservoir geologists and engineers. Potential reservoir rocks in the Ferron are generally subdivided on the basis of depositional setting and the relative position of the shoreline.

Stratigraphic architecture and depositional characteristics of the Ferron are outlined by Ryer (1981), Barton (1994), Gardner (1992, 1995) and Garrison *et al.* (1997). The Ferron is subdivided into seven units (or 'parasequence sets' using the terminology of Van Wagoner *et al.* 1990) by Ryer (1981), referred to as Genetic Sequences 1–7 (labelled GS1–GS7). GS1, GS2 and GS3 are interpreted as progradational, in which the relative sea level was constant or falling; GS4 and GS5 are interpreted as aggradational, in which the relative sea-level rise balances sediment input; GS6 and GS7 are interpreted as retrogradational, in which the relative sea-level rise outpaces sediment input.

Barton (1994) and van den Bergh and Garrison (1996, paper presented at Rocky Mountain Section Meeting, American Association of Petroleum Geologists) have proposed that reservoir characteristics of sandstone bodies are dependent not only on depositional setting, but are also controlled by allo-cyclic changes in accommodation and sediment supply. They concluded that, in addition to sand-prone proximal delta front sandstone units, distributary channels are the most significant reservoir elements in the Ferron. In meandering channel deposits, mudstone barriers occur along cross-beds, or lateral accretion surfaces of point bars (Bridge and Leeder 1979). At Corbula Gulch, which lies in the marine-influenced delta-plain portion of GS7, inclined cross-bedding is particularly well developed, and is well exposed along the two (nearly orthogonal) cliff faces (Figs 2 and 3), thus providing an excellent example of this class of channelized, meandering distributary channels. Four channel deposits (CDs) identified within the sandstone

**Figure 2** Topographic survey results (a) and GPR line and grid layouts (b). All 3D locations were obtained with GPS and lasergun. In (b) CG1–CG10 are the locations of stratigraphic sections measured down the cliff faces for use as constraints on the GPR interpretation. Cores from four holes (labelled W3, W4, W5 and W6) are also used as constraints. The view in (a) is towards the NW.



body are referred to as CD1–CD4, in ascending stratigraphic order (Fig. 4). We concentrate here on imaging a set of lateral accretion beds in CD2. Figure 5 shows examples, from the cores, of the range of lithologies present. These include cross-bedded sands, mud drapes and mudstone intraclast conglomerates. With this background, we can proceed to investigate the response of the site to GPR.

## GPR DATA ACQUISITION AND PROCESSING

All the GPR data (2D, 3D and borehole) are acquired with a PulseEKKO IV GPR system, manufactured by Sensors and

Software, Inc. Although tests were also performed at 50 MHz and 200 MHz, the surface GPR data are acquired primarily with 100 MHz half-wave dipole antennae, a 1000 V transmitter pulse, a time sample interval of 1.6 ns, a vertical stack of 64 traces at each location, a total recording time window of 400 ns, and 3 m separation between the transmitting and receiving antennae.

Surface GPR data are acquired at three grid scales to image the structures from submetre to regional dimensions. The largest scale survey consists of two sets of orthogonal lines, each 75 m apart, over an area  $650 \times 450$  m (Fig. 2). Traces were collected every 0.5 m along each line, giving a total of 11 486 traces in approximately 6 km of line to image the entire regional setting.

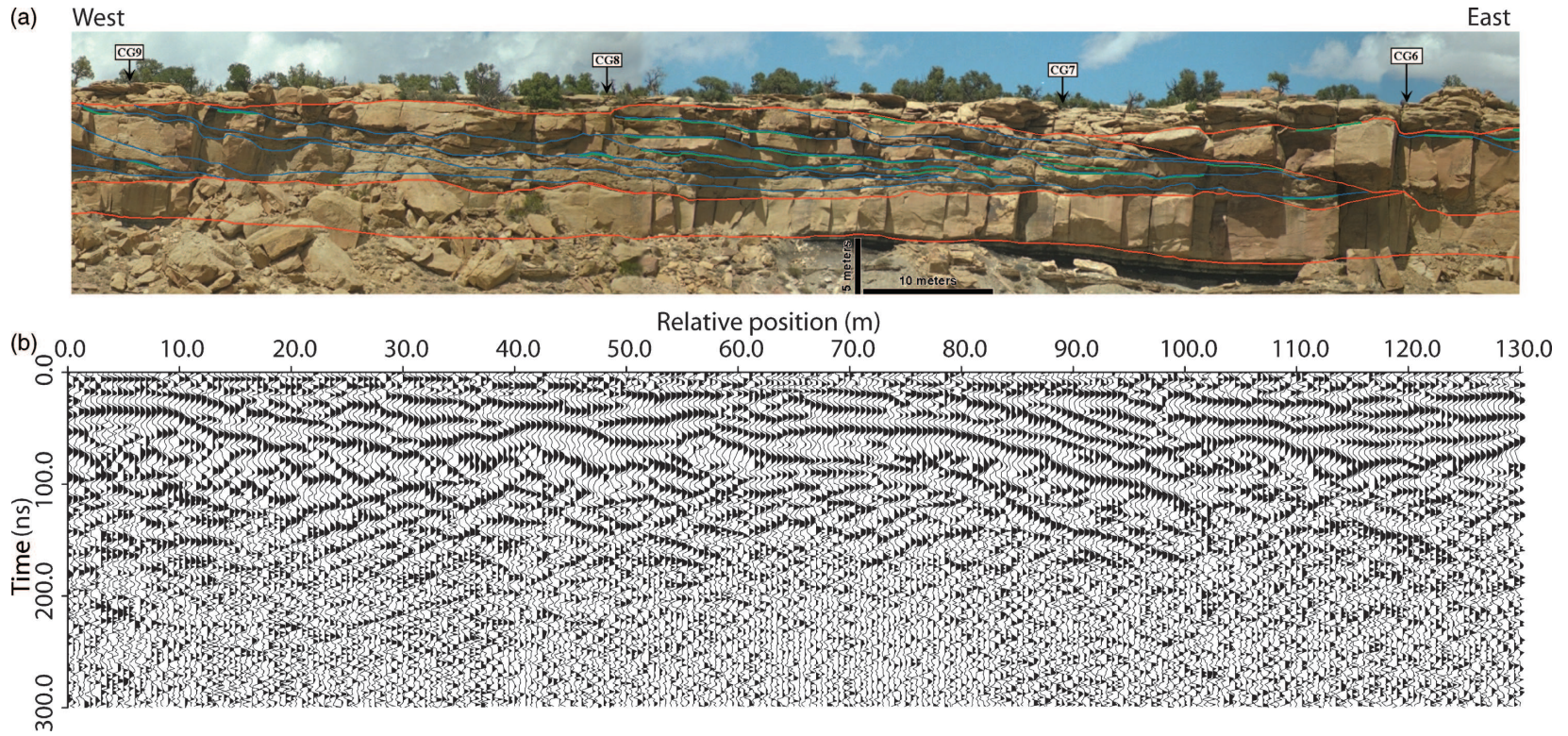


**Figure 3** Representative photomosaic of the south cliff exposure (a) showing the lateral accretion set. The same features are seen in the GPR data (b), which were acquired between CG9 and CG6 (Fig. 2) near the south edge of the mesa.

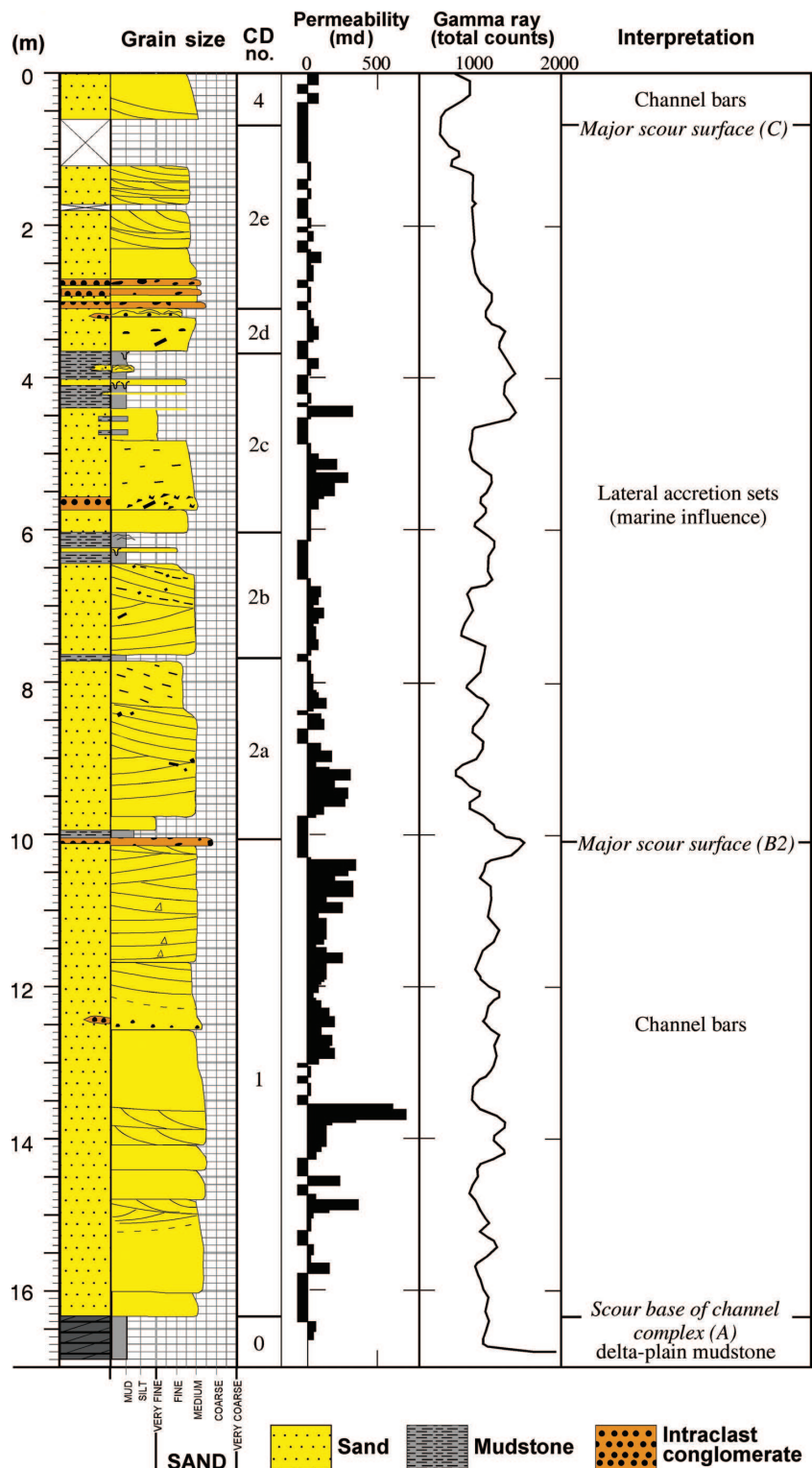


Figure 4 Representative core log (from Well 4); see Fig. 2(b) for location. Inability to measure permeability because of incompetence of the core (especially for mudstones) is indicated by assigning a negative permeability value.



**Figure 5** Representative core examples of the main lithologies at Corbula Gulch: (a) is between 7.3 and 7.9 m depth in hole 4 and shows cross-bedded sands and a clay drape within CD2; (b) is between 15.2 and 15.8 m depth in hole 5 and shows mudstone interclast conglomerate in CD1, just above the basal flood-plain mudstone. The diameter of the core is  $\sim 6.3$  cm (2.5 inches).

At an intermediate scale, a  $100 \times 150$  m grid of orthogonal lines with a 10 m line spacing (Fig. 2) was recorded to image complete lateral accretion beds. If the geometry and permeability of a single element can be defined, a reservoir scale model can be constructed by replication of this element. On this intermediate grid, a 0.25 m station spacing is used on the

16 NS lines and a 0.5 m spacing is used on the 12 WE lines. There is a total of 8824 traces in this data set.

Two 3D grid locations are shown in Fig. 2. Grid A is at the eastern edge of the mesa and grid B is at the southern edge. Both are orientated parallel to the local cliff faces. Grid A is  $27.0 \times 31.0$  m; grid B is  $28.0 \times 51.5$  m. The line and station spacing in both grids are 0.5 m, so grid A contains  $55 \times 63 = 3465$  traces and grid B contains  $57 \times 104 = 5928$  traces. We concentrate in this paper only on the two 3D volumes; the other data provide regional constraints and connections between the volumes.

A variety of borehole data are also acquired. These include vertical profiles in each hole to measure vertical velocity profiles, a constant depth cross-hole scan to measure the average horizontal velocity between holes 3 and 4, a full tomographic survey between holes 3 and 4 to image the 2D velocity distribution, and a surface survey tie-line (with a 10 cm station spacing) between holes 3 and 4. The results of analysis of these borehole data are included in the models presented below, but the details of the processing and the results are presented elsewhere (Hammon *et al.* 2002). A network of other surface tie-lines between the holes and the stratigraphic sections at the cliff face are also recorded (Fig. 2).

A line from the 3D grid A is shown in Fig. 6. This is plotted at various stages of the preprocessing to show the effects of time corrections, direct air- and ground-wave removal, median filtering to remove spikes, (31.25–125.0 MHz) band-pass filtering, and a three-trace mix. This same preprocessing is applied to all the surface GPR data.

## GPR VELOCITY ANALYSIS AND COMMON-OFFSET KIRCHHOFF MIGRATION

### Velocity model building

Velocity model building starts with the 2D tie-line between boreholes 3 and 4 (Fig. 2). This line also connects the two 3D GPR volumes. We begin by identifying the same units in the two core logs based on the observed lithology, the overall sediment dips and the geometry seen in the GPR tie-line. Then we connect the layers between the two boreholes to make an initial 2D model. The 2D interval velocity distribution is then obtained iteratively by matching the migrated depth section with the core logs. This 2D model is then used as an initial model for 2D tomography (Hammon *et al.* 2002). Additional 2D models are similarly constructed on four other tie-lines

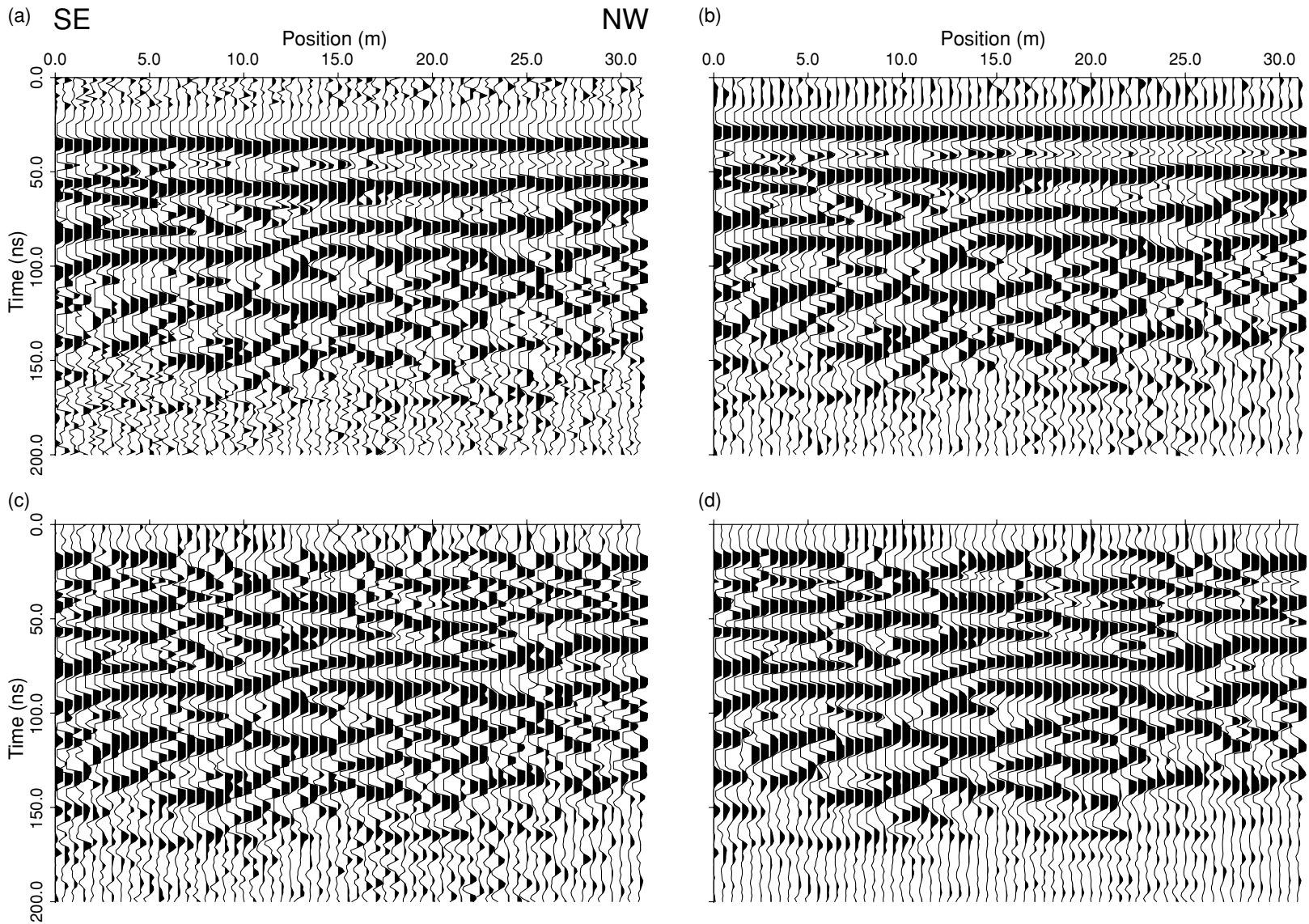
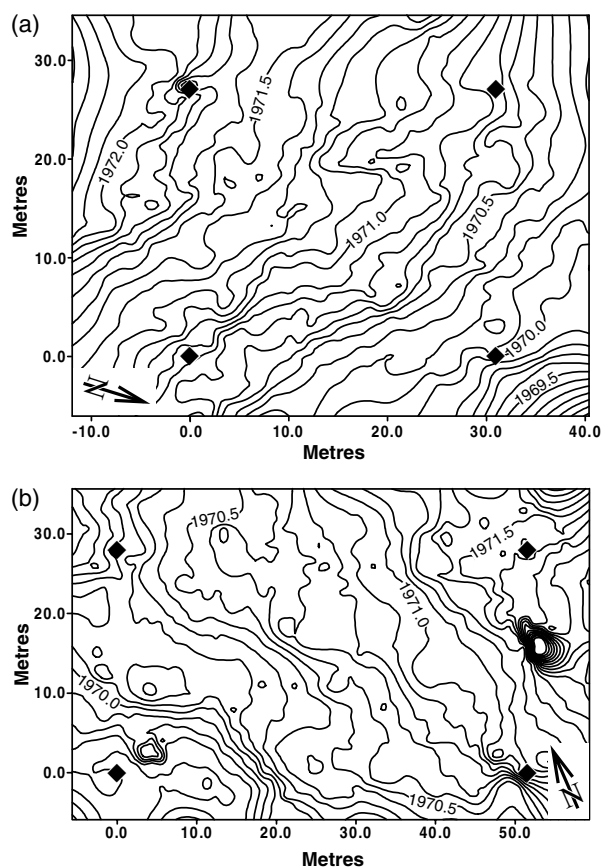


Figure 6 GPR data preprocessing: (a) shows the raw field data; (b) is after time corrections; (c) is after air-wave and ground-wave subtraction; (d) is after filtering. These steps are applied to all the surface GPR data. This line is the one nearest the east cliff face in 3D grid A (see Fig. 2).

between holes 3 and 4 and the locations of the cliff face stratigraphic sections CG8, CG7 and CG4 (Fig. 2).

These 2D velocity models are then interpolated and extrapolated to form a composite 3D velocity model. The contribution of any 2D velocity slice to a 1D velocity profile at any location in the 3D volume is defined by weighted averaging that is inversely proportional to the perpendicular distance between the slice and the profile. If the projection point is beyond the ends of the 2D line, data at the nearer endpoint are used. Separate interpolations are carried out for each CD using the boundaries as constrained by iterative migration, as described above. Interpolation and extrapolation are consistent with regional dip. The resulting 3D velocity model is fairly laterally homogeneous; the average vertical interval velocity down to 15 m depth is 0.101 m/ns, with a low-velocity zone of  $\sim 4$  m depth (Hammon *et al.* 2002).



**Figure 7** Surface topography over the two 3D GPR grids: (a) is for grid A; (b) is for grid B. Contours are in metres, with a contour interval of 10 cm. The uncertainty in GPS-determined locations is 2–4 cm horizontally and 4–5 cm vertically (C. Aiken 2003, pers. comm.). The black diamonds are the GPR grid corner points.

### 3D depth migration

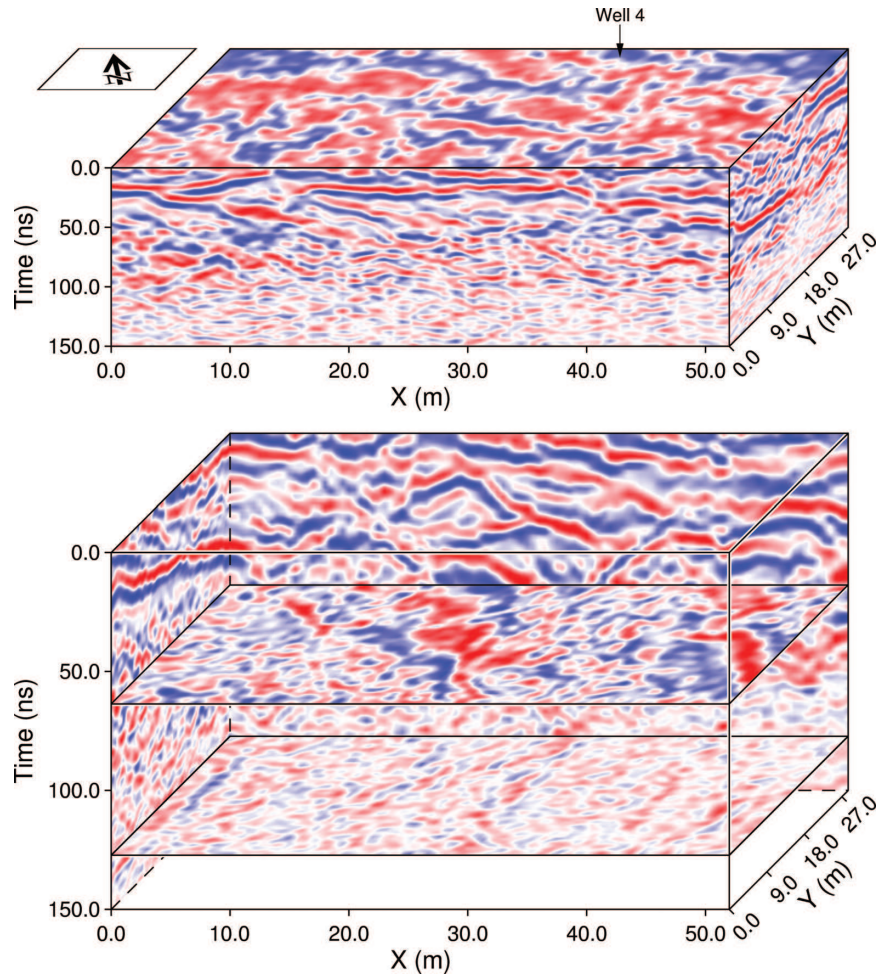
The 3D depth Kirchhoff migration algorithm used for the common-offset GPR data is that described by Epili and McMechan (1996); it builds a 3D volume as a series of slices. The 3D ray tracing uses the 2-point algorithm of Um and Thurber (1987). The algorithm is adapted for a cluster computing environment as described by Zeng and McMechan (2002). Ray tracing for the migration is carried out from each actual transmitter and receiver location, so elevation static corrections are not needed. This requires accurate topographic information (Fig. 7). The migration used an angular aperture in which the amplitude is tapered with a linear weighting function from 1 at  $20^\circ$  to 0 at  $60^\circ$ . The final images have a grid increment of 3.33 cm in all three directions. Figure 8 shows the 3D input common-offset GPR data volume and two fixed-time slices for 3D grid B. Figure 9 shows a similar display for these same data after 3D depth migration. Figure 10 contains slices through the depth migrated image of the data for grid A. The migrated depth volumes are post-processed with a  $0.16\text{--}3.0\text{ m}^{-1}$  vertical wavenumber filter, a median filter, and a horizontal trace mix in a  $1.0 \times 1.0$  m bin. Individual surfaces are correlated through and extracted from these volumes and from the intermediate and regional scale data sets to produce a sedimentological interpretation (Corbeanu 2001; Xu *et al.* 2001).

### 3D permeability model building

Probe permeameter measurements (Hurst and Goggin 1995) are made using a computer-controlled, stage-mounted, electronic probe permeameter at the University of Utah. Up to 2.74 m (9 ft) of continuous core (in 0.914 m (3 ft) segments) are tested in a single run. A steady-state method is applied using nitrogen gas as the permeant. A volume of approximately  $1\text{ cm}^3$  is tested using the 3 mm diameter tip. A 5 cm test spacing was employed along the core, except where core is missing or damaged. Regular calibration of the equipment is accomplished by frequently testing a set of permeability standards that cover a broad range of permeability values. The minimum value of permeability that can be resolved is  $\sim 1$  md.

The final step in the construction of the reservoir analogue is the estimation of the 3D distributions of fluid permeability. The method for carrying out this prediction is based on empirical relationships between the GPR attributes of instantaneous amplitude and instantaneous frequency, and the measured permeability values from the cores and cliff faces. The correlation between parameters is defined

**Figure 8** GPR data for 3D grid B. The upper panel shows the common-offset data volume; the lower panel shows fixed-time slices through the volume at 64 ns and 128 ns. The front of the cube is the side closest to the south cliff face. The result of depth migration of these data is shown in Fig. 9.



at the hole locations, and is then used to predict permeability values throughout the 3D volumes (Corbeanu *et al.* 2002). A separate but similar procedure is performed to predict the distribution of mudstone layers (Fig. 11). The latter are not well predicted by the permeability model, even though the mudstones are of low permeability. The reason for this is that the relevant data are scarce because the mudstones tend to crumble before their permeability can be measured (see the gaps indicated by the negative values in the permeability profile in Fig. 4).

Representative slices through the predicted 3D permeability/mudstone volumes are shown in Fig. 12 for grid A and in Fig. 13 for grid B. The average permeability in CD2 (above  $\sim 10$  m depth) is  $\sim 37$  md; the average in CD1 (below  $\sim 10$  m depth) is  $\sim 52$  md. These models can be input to fluid-flow simulations for reservoir evaluation; simulations are beyond the scope of the present paper, but are presented by Novakovic *et al.* (2002). Although there are near-vertical fractures present

(e.g. Fig. 2a) and these will dominate the fluid-flow patterns, we have limited our consideration to only the lithology-related permeability, as the former are not well detected by the near-vertically propagating GPR waves.

## SYNOPSIS

3D processing of 3D GPR data from ancient clastic sequences provides insight into their internal architecture. The geometries and extents of individual features are revealed; detailed sedimentological interpretation is given by Corbeanu *et al.* (2004). This involves a tight integration of the geophysical (GPR), geological (lithologic sections, bounding surfaces and structure) and petrophysical (permeability) data. Each data type adds salient constraints to the interpretation of the others. The final model is a deterministic 3D representation of the features that control fluid flow (in contrast to most previous models, which are statistical).

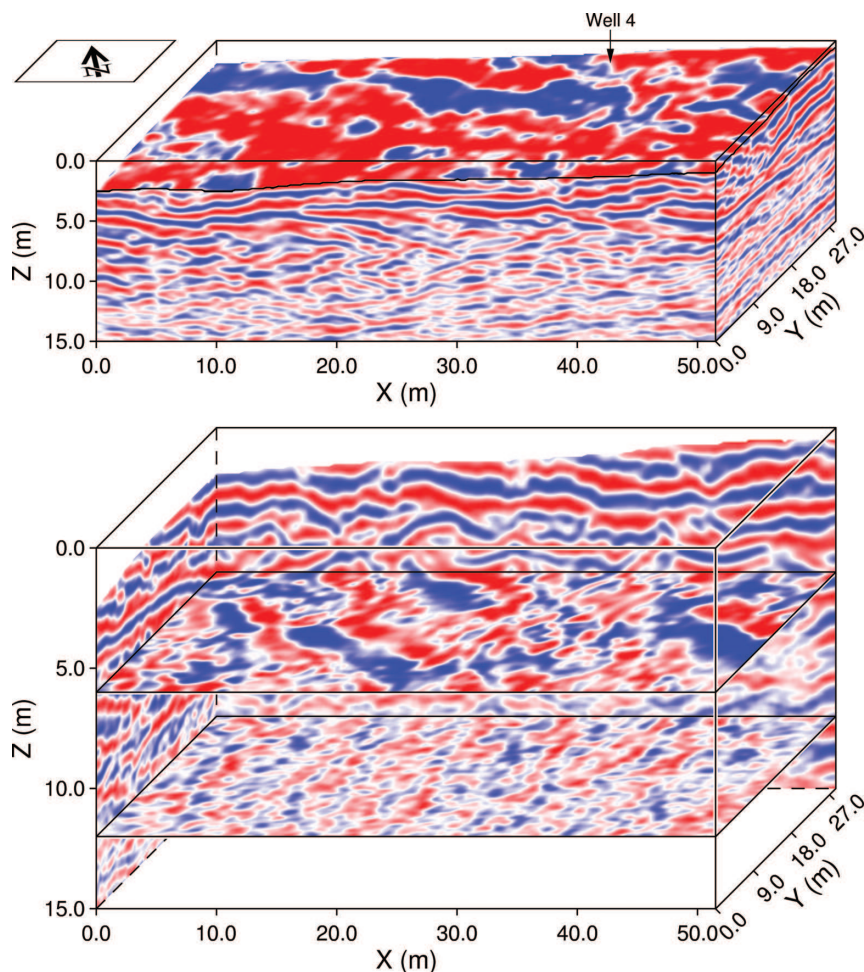


**Figure 9** A common-offset 3D migration of the data in grid B. The upper panel shows the migrated data volume; the lower panel shows fixed-depth slices through the volume at 6 m and 12 m depths. The upper surface of the migrated image in the upper panel is the earth's topographic surface. The front of the cube is the side closest to the south cliff face. The input data volume is shown in Fig. 8.

## ACKNOWLEDGEMENTS

The research leading to this paper was funded by the U.S. Department of Energy under Contract DE-FG03-96ER14596. Mike Wizevich guided the initial sedimentological mapping of the site. The permeability measurements were performed by Craig Forster and Steve Snelgrove at the University of Utah. Constructive comments by reviewers Roger Young and Charles Young and by the Associate Editor Jan van der Kruk are appreciated. This paper is Contribution No. 1005 from the Department of Geosciences of the University of Texas at Dallas.

## REFERENCES

- Barton M.D. 1994. *Outcrop characterization of architecture and permeability structure in fluvial-deltaic sandstones, Cretaceous Ferron sandstone, Utah*. PhD dissertation, University of Texas at Austin.
- Bridge J.S. and Leeder M.R. 1979. A simulation model of alluvial stratigraphy. *Sedimentology* **26**, 617–644.
- Corbeanu R.M. 2001. *3D architecture of ancient delta plain channels in the Cretaceous Ferron Sandstone, Utah*. PhD dissertation, University of Texas at Dallas.
- Corbeanu R.M., McMechan G.A., Szerbiak R.B. and Soegaard K. 2002. Prediction of 3D fluid permeability and mudstone distributions from ground-penetrating radar (GPR) attributes: Example from the Cretaceous Ferron Sandstone member, east-central Utah. *Geophysics* **67**, 1495–1504.
- Corbeanu R.M., Wizevich M.C., Bhattacharya J.P., Zeng X. and McMechan G.A. 2004. Three-dimensional architecture of ancient lower delta-plain point bars using ground-penetrating radar, Cretaceous Ferron Sandstone, Utah. In: *The Fluvial-Deltaic Ferron Sandstone: Regional-to-Wellbore-Scale Outcrop Analog Studies and Applications to Reservoir Modeling* (eds T.C. Chidsey, R.D. Adams and T.H. Morris). American Association of Petroleum Geologists Memoir, in press.
- Epili D. and McMechan G.A. 1996. Implementation of 3D prestack Kirchhoff migration, with application to data from the Ouachita frontal thrust zone. *Geophysics* **61**, 1400–1411.
- Gardner M.H. 1992. Sequence stratigraphy of the Ferron Sandstone, east-central Utah. In: *Architecture and Permeability Structure of Fluvial-Deltaic Sandstones: A Field Guide to Selected Outcrops of*

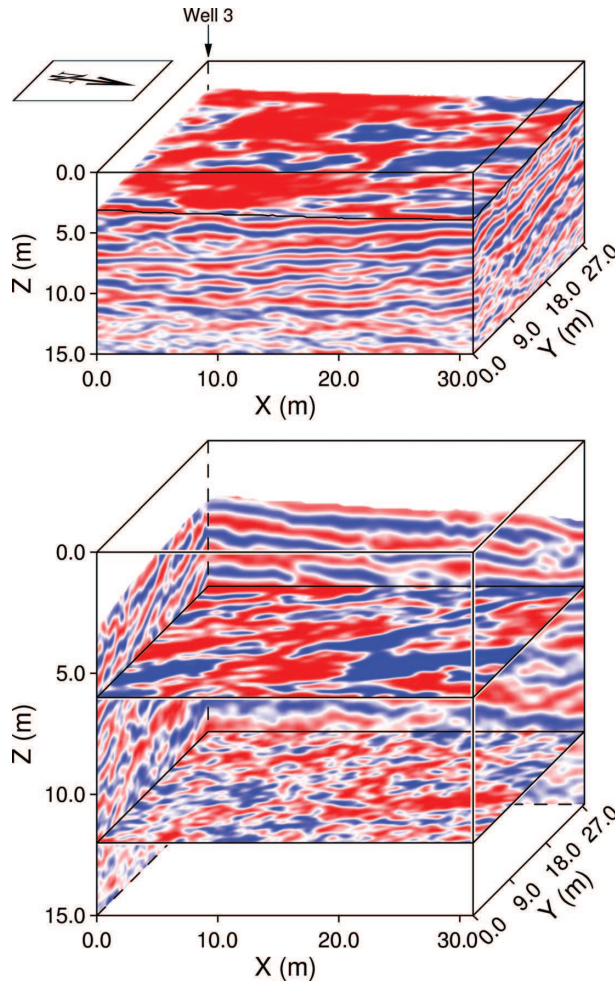


**Figure 10** Common-offset 3D migration of the data in grid A. The upper panel shows the migrated data volume; the lower panel shows fixed-depth slices through the volume at 6 m and 12 m depths. The upper surface of the migrated image in the upper panel is the earth's topographic surface. The front of the cube is the side closest to the east cliff face.

*the Ferron Sandstone, East-Central Utah* (eds N. Tyler, M. Barton and R.S. Fisher), pp. 1–12. Bureau of Economic Geology, University of Texas at Austin.

Gardner M.H. 1995. Tectonic and eustatic controls on the stratal architecture of mid-Cretaceous stratigraphic sequences, central western interior foreland basin of North America. In: *Stratigraphic Evolution of Foreland Basins* (eds S.L. Dorobek and G.M. Ross), pp. 243–281. Society of Economic Paleontologists and Mineralogists, Special Publication 52.

- Garrison J.R. Jr, van den Bergh T.C.V., Barker C.E.F. and Tabet D.E. 1997. Depositional sequence stratigraphy and architecture of the Cretaceous Ferron Sandstone: Implications for coal and coalbed methane resources – A field excursion. In: *Depositional Sequence Stratigraphy and Architecture of the Ferron Sandstone: Implications for Coal and Coalbed Methane Resources – A Field Excursion* (eds P.K. Link and B.J. Kowallis), pp. 155–202. Geological Society of America Field Trip Guidebook, 1997 Annual Meeting, *BYU Geology Studies* 42, part 2.
- Hammon III W.S., Zeng X., Corbeanu R.M. and McMechan G.A. 2002. Estimation of the spatial distribution of fluid permeability from surface and borehole GPR data and core, with a 2D example from the Ferron Sandstone, Utah. *Geophysics* 67, 1505–1515.
- Hurst A. and Goggin D. 1995. Probe permeametry: An overview and bibliography. *American Association of Petroleum Geologists Bulletin* 79, 463–473.
- Langley R.B. 1998. RTK GPS. *GPS World* 6, 70–76.
- Novakovic D., White C.D., Corbeanu R.M., Hammon III W.S., Bhattacharya J.P. and McMechan G.A. 2002. Effects of shales in fluvial-deltaic deposits: Ground-penetrating radar, outcrop observations, geostatistics, and three-dimensional flow modeling for the Ferron Sandstone, Utah. *Mathematical Geology* 34, 857–893.
- Ryer T.A. 1981. Deltaic coals of the Ferron Sandstone member of the Mancos Shale: Predictive model for Cretaceous coal-bearing strata of the western interior. *American Association of Petroleum Geologists Bulletin* 65, 2323–2340.
- Szerbiak R.B., McMechan G.A. and Corbeanu R.M. 2001. 3D characterization of a clastic reservoir analog: From 3D GPR data to a 3D fluid permeability model. *Geophysics* 66, 1026–1037.
- Um J. and Thurber C. 1987. A fast algorithm for two-point seismic ray tracing. *Bulletin of the Seismological Society of America* 77, 972–986.
- Van Wagoner J.C., Mitchum R.M., Campion K.M. and Rahmanian V.D. 1990. Siliciclastic sequence stratigraphy in well-logs, cores and outcrop. *American Association of Petroleum Geologists, Methods in Exploration Series* 7, 1–55.
- Xu X., Aiken C.L.V., Corbeanu R.M., Zeng X., McMechan G.A. and Bhattacharya J.B. 2001. High accuracy 3D digital integration, visualization, and analysis of geological data: Reservoir characterization of the Ferron Sandstone, Utah. In: *Integrated 3D Ground Penetrating Radar, Outcrop, and Borehole Data Applied to Reservoir Characterization and Flow Simulation* (eds G.A. McMechan, R. Corbeanu, C. Forster, K. Soegaard, X. Zeng, C. Aiken *et al.*). Final Report, Department of Energy Contract DE-FG03-96ER14596, The University of Texas at Dallas.
- Zeng X. and McMechan G.A. 2002. Load balancing across a highly heterogeneous processor cluster using file status probes, with application to 3D ray tracing for Kirchhoff depth migration. *Computers & Geosciences* 28, 911–918.

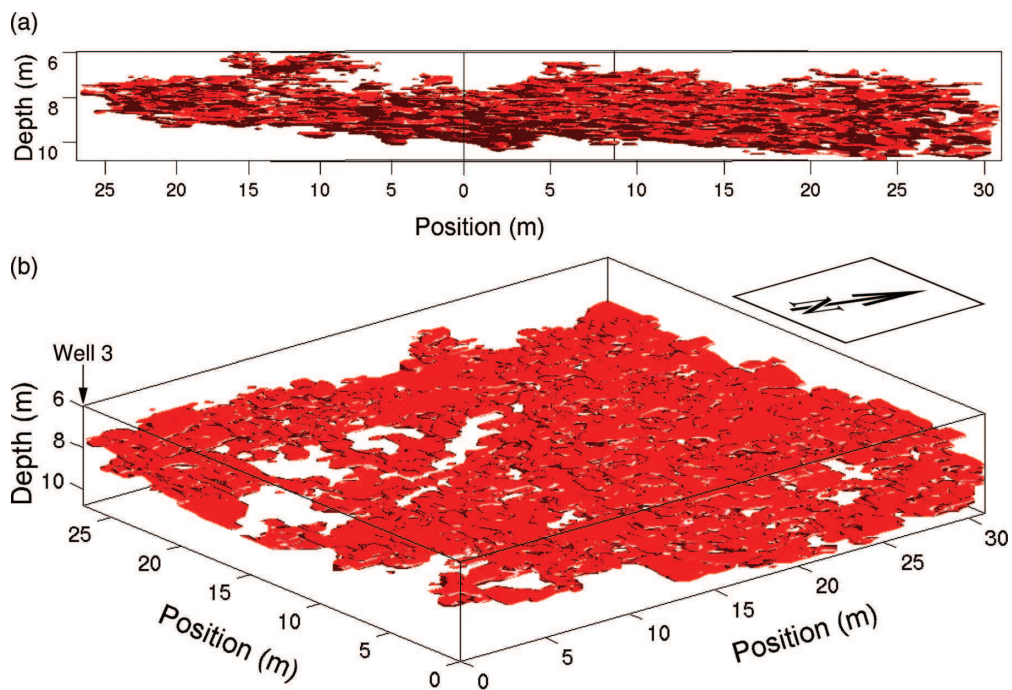


**Figure 11** Predicted mudstone distribution in the grid A volume. View (a) is rotated to be approximately in the strike direction. View (b) contains the same data as in (a), but is inclined to show the areal extent of the mudstone distribution.

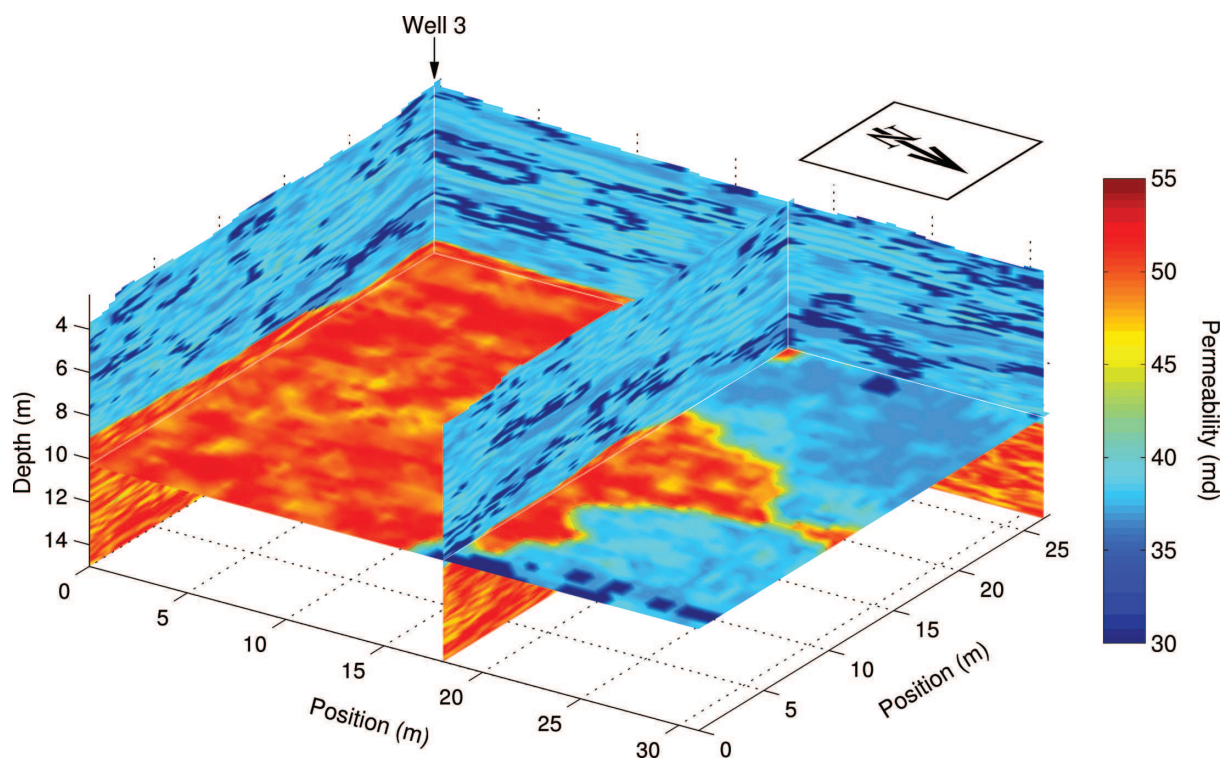


**Figure 12** Predicted permeability values for grid A. The dark blue values superimposed correspond to the predicted (low permeability) mudstones within CD2, as shown in 3D in Fig. 11. The red regions indicate high permeability within CD1. The horizontal slice is at 10.3 m depth.

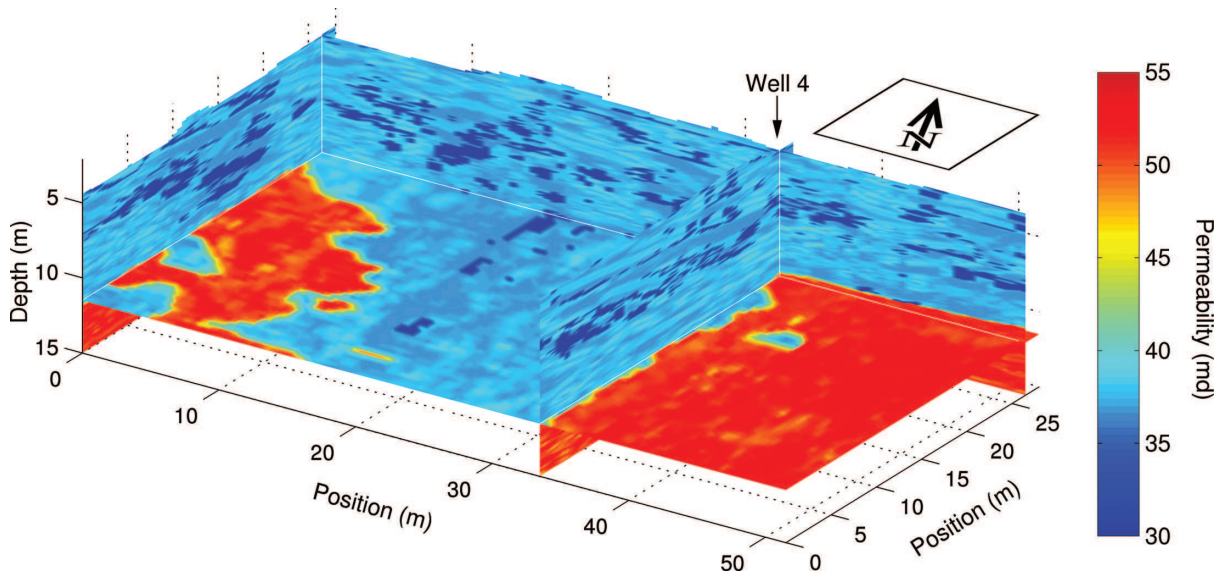


Figure 13 Predicted permeability values for grid B. The dark blue values superimposed correspond to the predicted (low permeability) mudstones within CD2. The red regions indicate high permeability within CD1. The horizontal slice is at 11.5 m depth.